Journal of
Composites Science

MDPI

Article

Preliminary Design Optimization of CFRP Crash Box for High-Performance Automotive Applications

Antonio Maria Caporale *, Alessandro Amato and Gerardus Janszen

Aerospace Science and Technology Department, Politecnico di Milano, 20156 Milan, Italy
* Correspondence: antoniomaria.caporale@polimi.it

Abstract

This study presents a hybrid experimental–numerical methodology for the preliminary design and optimization of a CFRP crash box intended for high-performance automotive applications. An initial experimental campaign was conducted on frustum-shaped crash boxes manufactured by Pagani Automobili S.p.A., comparing constant and variable thickness configurations through drop tower impact tests to evaluate energy absorption, crushing stability, and failure mechanisms. A lightweight finite element model was developed in Abaqus/Explicit using shell elements and Hashin-based damage criteria, achieving calibration errors below 10% for most parameters and under 15% for peak forces. Geometric enhancements, including continuous flanges, removal of the top surface, and an internal cruciform reinforcement, significantly improved energy absorption (up to 110%) but introduced trade-offs in stroke efficiency and mean force levels. To mitigate these effects, a genetic algorithm was employed to optimize laminate layup by varying ply orientations, resulting in improved stroke efficiency and reduced peak and average forces while maintaining crushing stability. The proposed approach demonstrates that integrating experimental validation with efficient numerical modeling and optimization accelerates the development of lightweight, high-performance crash absorbers, offering a robust framework for motorsport and automotive applications that balances safety, efficiency, and manufacturability.

Keywords: impact absorption; crashworthiness; high-performance automotive; composite crushing; crushing modelling

Academic Editor: Jacob Aboudi

Received: 9 December 2025
Revised: 30 January 2026
Accepted: 5 February 2026
Published: 11 February 2026

1. Introduction and Objectives

Passive safety represents a fundamental pillar in motorsport engineering, where vehicles operate under extreme speeds and dynamic loads that pose significant risks to drivers. Continuous advancements in crash structures, energy-absorbing composites, and restraint systems have markedly reduced the probability of severe injuries during high-impact events. Beyond safeguarding professional drivers, these innovations serve as critical platforms for validating novel concepts of structural integrity under extreme conditions.

In this context, composite crash absorbers play a decisive role in mitigating the consequences of high-energy impacts in racing vehicles. The most common examples are the nose, side, and rear crash boxes, each specifically designed to protect critical areas of the vehicle and the driver. The nose cone, mounted at the front, is engineered to crush in a controlled manner during frontal collisions, dissipating energy before it reaches the survival cell. Side structures are optimized to absorb loads from lateral impacts, which are particularly dangerous due to the limited energy absorption stroke available. Rear crash

boxes, positioned behind the gearbox, mitigate the forces generated in rear-end accidents, preserving both the car's integrity and the driver's safety. All these components are engineered with geometries and material layouts that guarantee a progressive and predictable collapse mechanism.

The effectiveness of composites in these applications lies in their unique crushing behavior. Unlike ductile metals, which primarily absorb energy through plastic deformation, fiber-reinforced composites dissipate energy through a complex sequence of damage mechanisms. These include matrix cracking, fiber breakage, delamination, and the frictional sliding of crushed plies, all of which contribute to the highly efficient and progressive absorption of kinetic energy. By tailoring the fiber orientation, laminate stacking sequence, and wall thickness, engineers can design crash boxes that fail in a stable and controlled way, avoiding brittle fracture and ensuring consistent performance across different impact scenarios. Moreover, composites offer an exceptional strength-to-weight ratio, allowing safety structures to remain lightweight without compromising their protective capacity.

A comprehensive review of the state of the art of automotive crash boxes was published in 2017 [1]. Recent research works focus on innovative manufacturing techniques for composite crash boxes such as UV-pultrusion [2], 3D-printed structures with CFRP reinforcement [3], and 3D printed composites [4]. Research on different composite materials, such as glass-fiber [5,6], thermoplastic [7], graphene-filled materials [8], and multi-material laminates [9], was performed, as well as on different filler configurations like foam-filled crash boxes [10] or metamaterial or lattice-based [11], chiral [12], strut-based [13], or with cellular section [14]. Different geometries and topologies were investigated such as multi-corner [15], origami [16–18], or bio-inspired [19]. A parametric study on geometry and layup were performed in [20].

The design and optimization of composite crash absorbers greatly benefit from explicit finite element (FE) simulations, which allow engineers to capture the highly dynamic and nonlinear response of these structures under impact. Explicit solvers are particularly suited for modeling progressive crushing, as they can reproduce the complex sequence of failure mechanisms and energy dissipation observed experimentally. This capability enables the virtual assessment of different geometries, layups, and boundary conditions without the need for extensive physical testing, accelerating the development process. However, the numerical modeling of composite crushing poses several challenges. Accurate predictions require fine mesh discretization, robust failure criteria, and advanced material models capable of representing intralaminar and interlaminar damage, frictional effects, and contact instabilities. These aspects make simulations computationally expensive and sensitive to modeling assumptions. Furthermore, ensuring numerical stability while avoiding artificial energy contributions remains a delicate task, demanding a careful balance between model fidelity and efficiency. Two reviews on the numerical methods for composite crushing modeling were published in 2022 [21,22]. The modeling techniques can be classified depending on the fidelity level. Low-idealization-level high-fidelity approaches have been developed that model the intralaminar and interlaminar damages at the level of single ply [23,24], also in the case of thermoplastic matrix [25], for tubes [26] and wave beams [27,28], showing extremely accurate modeling capacity. Conversely, low-fidelity approaches are characterized by a higher degree of idealization, which results in lower accuracy but offers a significant advantage in terms of computational efficiency. These models typically rely on shell elements to approximate the behavior of the laminates or portions of them. Stacked shell models incorporate the behavior of each interlamina in a single cohesive property (elements or contacts) between two layers of shell elements, which represent half of the laminate each [29]. Single-shell models do not directly model delaminations but consider their energetical contribution by artificially increasing the in-

plane fracture toughness. As a part of this family, it is worth mentioning the CZone module for Simulia/Abaqus [27,30,31]. This tool exploits a calibrated contact law that reproduces the force experienced by the structure during crushing without inducing actual element deformation, thereby avoiding distortion issues that are typical of single-shell approaches.

Recently, data-driven and machine learning approaches were adopted in the performance optimization of crash boxes. For example, in [32], Physically Informed Neural Networks were used to optimized the geometry of an origami crash box, but also Gaussian Process Regression [15] and the Mapping Method on polynomial surrogate model [33], compared with the Radial Basis Function [34], were adopted for the same scope. Multi-Design Optimization [35] was used to improve the energy absorption of tubes filled with honeycomb or foam [36–39].

This work aims to assess a hybrid experimental–numerical procedure for optimizing the performance of a CFRP energy-absorbing structure, representative of the rear crash box in a high-performance vehicle. The goal is to validate a lightweight computational model for optimizing the geometry and lamination sequence of the structure. Data from the initial experimental impact tests will be used to develop a highly idealized numerical model, capable of delivering reliable predictions with a reduced computational cost. This calibrated model will first be employed to explore potential geometric improvements and subsequently to perform a genetic algorithm-based optimization of the lamination sequence. Finally, the complex interplay among performance parameters, such as the specific energy absorption, mean force, and stroke efficiency, will be analyzed to identify an optimal configuration.

2. Experimental Testing

2.1. Methods and Specimens

An experimental impact testing campaign was carried out using a vertical sled on frustum-shaped composite crash boxes with a linearly variable rectangular cross-section and a closed upper end. The specimens, manufactured by Pagani Automobili S.p.A. (San Cesario Sul Panaro, Italy), are meant to be representative of a real crash box, thus incorporating all the functional elements but with a simplified shape, to reduce the manufacturing complexity in the preliminary testing phase. They were investigated with two main objectives: (i) to assess the energy-absorption capacity, crushing behavior, and dominant damage mechanisms of different absorber configurations; and (ii) to calibrate a numerical model for subsequent geometric and layup optimization.

For the initial characterization, a total of five specimens were tested: three with a constant thickness along the height, consisting of eight plies, and two with a tapered configuration, featuring a gradual reduction in the number of plies through the thickness along the length. In the tapered specimens, the base section comprises eight plies, while the third, fifth, and seventh plies are terminated at 110 mm, 120 mm, and 130 mm from the base, respectively. The crash box base includes two lateral flanges, each with two holes designed to accommodate screws for fastening the specimen to a steel plate, ensuring proper fixation during testing. The specimen geometry and a schematic of the tapering configuration are shown in Figure 1c.

The specimens were manufactured using two types of commercially available carbon/epoxy prepreg fabrics, adopting an IMP503Z-HT epoxy matrix, and subsequently molded through an autoclave process. The two fabrics differ in their weave architecture: the first fabric, referred to as “A”, features a 2 × 2 twill weave resulting in a cured ply thickness of 0.42 mm, whereas the second, referred to as “B”, adopts a plain weave weave resulting in a cured ply thickness of 0.32 mm. The stacking sequences for the specimens with constant (C) and variable (V) thickness configurations are reported in Tables 1 and 2,

respectively. It is worth noting that the orientation angles are defined, in each case, with respect to the projection of the longitudinal axis on the corresponding ply plane.

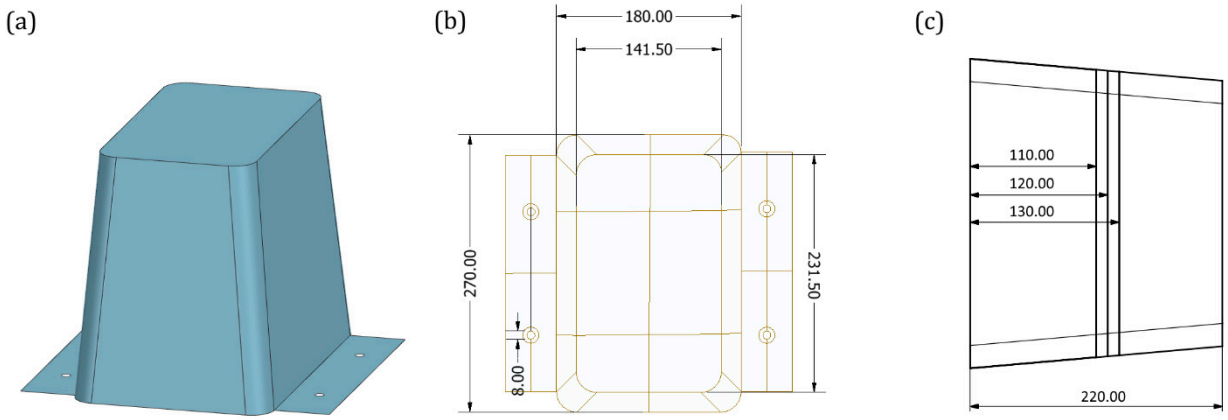

Figure 1. Original geometry of constant and variable-thickness specimens. All dimensions are reported in mm. (**a**) External shape, (**b**) top view, and (**c**) lateral view with tapering detail.

Table 1. Constant thickness specimens lay-up, from outer to inner layers.

	Region	Fabric	Orientation
Ply-1	Total (with flanges)	A	45°
Ply-2	Total (with flanges)	B	0°
Ply-3	Total (with flanges)	B	45°
Ply-4	Total	B	0°
Ply-5	Total	B	0°
Ply-6	Total	B	0°
Ply-7	Total	B	45°
Ply-8	Total	A	45°

Table 2. Variable thickness specimens layup, from outer to inner layers.

	Region	Fabric	Orientation
Ply-1	Total (with flanges)	A	45°
Ply-2	Total (with flanges)	B	0°
Ply-3	From flanges to 110 mm	B	45°
Ply-4	Total	B	0°
Ply-5	Up to 120 mm	B	0°
Ply-6	Total	B	0°
Ply-7	Up to 130 mm	B	45°
Ply-8	Total	A	45°

A six-meter-tall drop tower was employed to perform the impact tests (see Figure 2a), using a 300 kg impact mass accelerated by gravity and guided by two lateral rails. The mass was raised with an electric hoist and released upon receiving the trigger signal, which simultaneously initiated the acquisition from two Phantom VEO-E 310L high-speed cameras, one for the frontal view and one for a lateral view, and the accelerometer mounted on the impacting mass. This accelerometer was acquired with a frequency of 20 kHz and filtered with a 1000 Hz low-pass filter to avoid spurious frequencies. A photocell was used to measure the impact velocity. A picture of the setup is shown in Figure 2b. To compare the performance of the different specimens and to evaluate the effectiveness of energy absorption, four key quantities were considered: *Specific Absorbed Energy* (SEA), *Crush Force*

Efficiency (CFE), *Stroke Efficiency* (SE), and *Maximum Force* (MF). While the definition of the last one is straightforward, the first three are defined as follows:

$$SEA = Absorbed\ Energy / Crushed\ Mass$$

$$CFE = Maximum\ Force / Average\ Force$$

$$SE = Crushed\ Stroke / Available\ Stroke$$

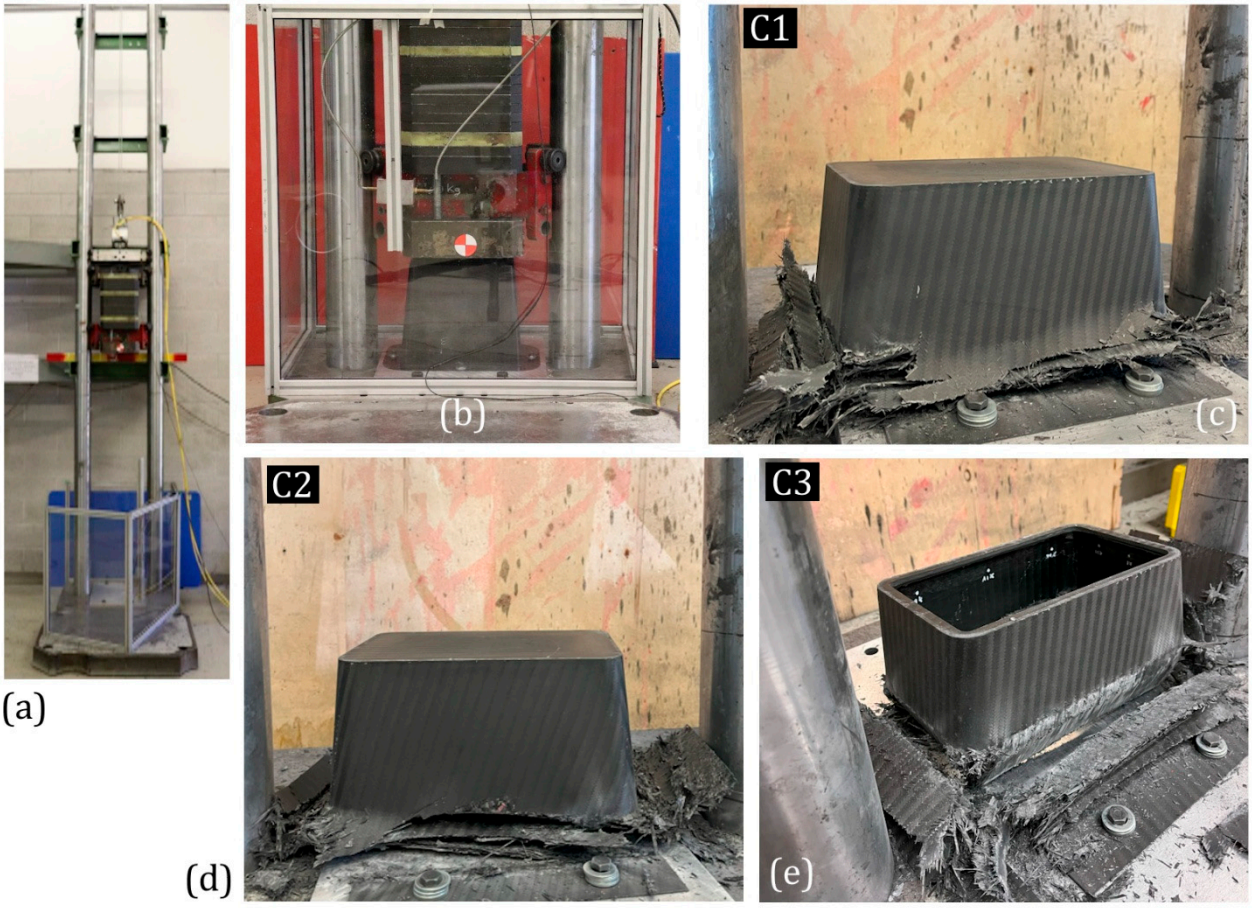

Figure 2. Impact test setup: (**a**) drop tower and (**b**) example of an impact test configuration. Post-impact specimens: (**c**) C1, (**d**) C2, and (**e**) C3.

Absorbed Energy is defined as the integral of the force vs. displacement curves. Crushed mass, needed to compute the SEA, was obtained by measuring the mass of the non-crushed residual of the crash box after the impact and subtracting it to the original mass.

2.2. Results—Constant Thickness

The first two specimens with constant thickness, C1 and C2, were tested in their as-manufactured condition. Their mass and test parameters are reported in Table 3. It is relevant to note the difference in weight between specimen C1 and C2, which have the same geometry and the same lamination sequence. This difference in mass should be addressed to undesired uncertainties and variabilities, in the manufacturing process, so that C2 has probably incorporated more resin than C1.

Both specimens exhibited quite stable crushing behavior, although it initiated from the bottom of the structure (inverse mode). The impact images (Figure 2c,d) suggest that this crushing mode was triggered by stress concentrations at the junction between the main body and the flanges. The composite progressively crushed, generating debris

ranging from fine powder to horizontal strips a few centimeters wide. This behavior may indicate the occurrence of local buckling at the crushing front, possibly related to the slightly inclined walls of the crash box. Indeed, a small inclination between the wall and the impacting surface introduces a bending moment within the wall, which could promote local buckling. Nevertheless, no evidence of global collapse, extensive cracking, or large-scale buckling was observed, confirming the effective energy absorption capability of the structure (Figure 2c,d).

Table 3. Constant-thickness specimens testing conditions.

Specimen	Mass g	Impact Mass kg	Impact Speed m/s
C1	990	300	8.2
C2	1030	300	8.2
C3	880	300	8.2

From these experimental observations, it was noted that the upper surface of the crash box had a limited contribution to the overall crushing behavior. In fact, its presence may even be detrimental to the performance, as it increases the bending stiffness of the uppermost portion of the lateral walls, thereby promoting the onset of inverse crushing. For this reason, the upper surface of specimen C3 was removed with a CNC milling machine, leaving a 10 mm wide frame only (see Figure 2e), thus reducing its mass from 1020 g to 880 g. Then, it was tested with the same configuration used for C1 and C2. The removal of the top surface did not alter the test outcome, which once again resulted in a quite stable and effective energy absorption but still exhibited inverse crushing, indicating that this change in configuration was effective only in reducing the weight. However, it was also observed that the contact between the specimen and the support plate was not uniform, as the flanges were not perfectly aligned with the lower section of the frustum cone due to the manufacturing complexities, leaving a small air gap between this edge and the plate. This misalignment produced stress concentration at the flange joints, which could trigger the inverse crushing.

The acceleration and force curves from the first three tests are shown in Figure 3a as a function of displacement and Figure 3b as a function of time. As before, the CFC60 filter was applied. The curves show quite a repeatable behavior with a first elastic response, followed by a recognizable crushing plateau, followed by the final load drop when the impactor is completely arrested.

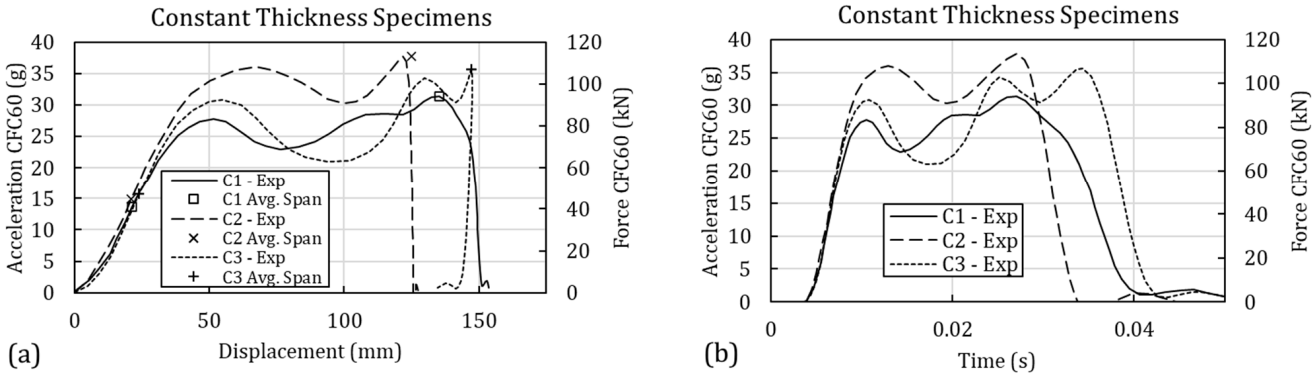

Figure 3. Deceleration curves of constant-thickness specimens, C1, C2, and C3, as a function of (**a**) displacement and (**b**) time.

The average crushing acceleration/force, together with the four performance parameters (SEA, MA, CFE, and SE), are summarized in Table 4. To obtain a reliable and repeatable

estimate of the average crushing force, a consistent criterion for defining the averaging span was adopted. In this study, the first inflection point of the acceleration curve, corresponding to the onset of the derivative decrease, was selected as the starting point, while the last local maximum before the final load drop was taken as the endpoint. The averaging span of the three curves are specified in Figure 3a.

Table 4. Performance parameters of constant-thickness specimens, C1, C2, and C3.

Specimen	Avg. Crushing Force kN	Max F kN	SEA kJ/kg	CFE kN/kN	SE mm/mm
C1	74.67 ± 12.58	92.21	13.77	0.810	0.70
C2	90.35 ± 18.52	111.32	16.52	0.812	0.58
C3	82.07 ± 15.32	104.94	19.92	0.782	0.67

The three specimens, C1, C2, and C3, showed a repeatable behavior in terms of these performance parameters too. Nonetheless, some points are interesting to note: the average crushing force of C1 is lower than the other two specimens. This could be related to the difference in mass among them (see Table 3), which could act on the crushing force both in terms of additional inertia and in thicker walls, thus higher buckling loads. C2, which has the higher average force, has, as a consequence, a lower Stroke Efficiency SE. Comparing the SEA, C2 showed a 20% increase compared to C1. If, as suggested by its higher mass, C2 had a higher resin content, then, the role of it in the increased SEA could be hypothesized. C3 showed a 20% higher SEA than C2, confirming the low relevance of the top surface in the energy absorbing mechanisms.

2.3. Results—Variable Thickness

Specimens V1 and V2 featured a variable number of plies and thus a variable thickness in their lateral surfaces, as shown in Figure 1c. This configuration was originally intended to have a reduced thickness in the top region of the absorber to reduce the initial force peaks, typically observed in the first phase of crushing, and ensuring a proper trigger. Specimen V1 was tested in its as-manufactured condition, while for V2, the upper surface was removed, as previously done for specimen C3. The test configuration parameters are reported in Table 5.

Table 5. Variable-thickness specimen testing conditions.

Specimen	Mass g	Impact Mass kg	Impact Speed m/s
V1	845	300	8.2
V2	751	300	7.0

Despite the tapering, the test of specimen V1 again resulted in inverse crushing, initiating at the flange joints. Furthermore, the structure collapsed in an unstable manner: one of the two larger lateral walls fractured into two large pieces due to a crack that appeared to originate a few centimeters above the tapering, as clearly visible in Figure 4b. Such inefficient crushing, characterized by large cracks instead of progressive composite fragmentation, led to inadequate energy absorption. As a result, the specimen was unable to stop the impactor, which caused its complete compaction and a severe deceleration peak.

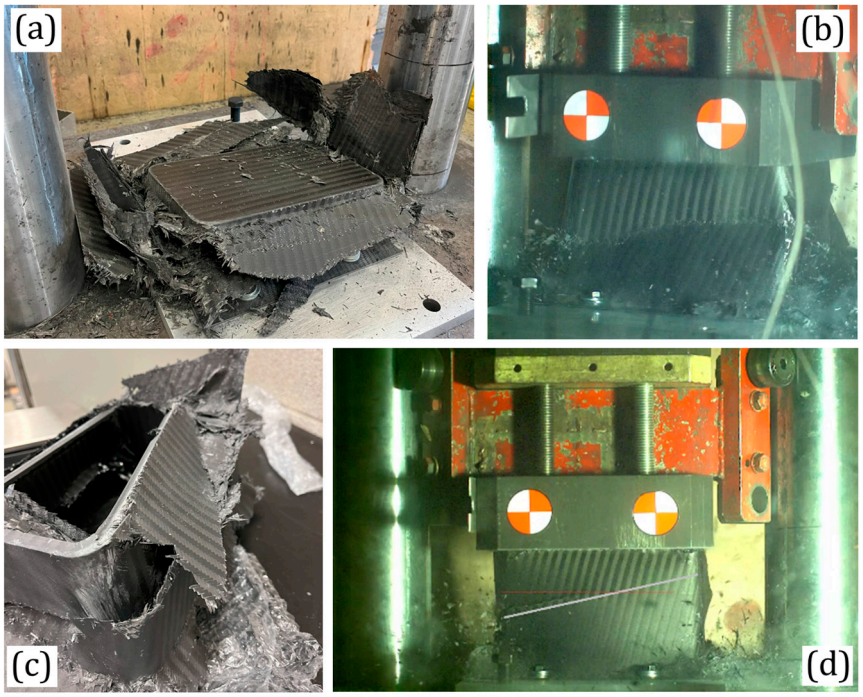

Figure 4. Crushing behavior of variable-thickness specimens, V1 and V2: (**a**) crushed V1 specimen and (**b**) primary collapse of its front face, (**c**) crushed V2 specimenand (**d**) collaps of its rear face.

The second variable-thickness specimen (V2) was tested under reduced impact energy compared to V1, to assess the effect of tapering while avoiding the full densification of the specimen. Moreover, the top surface was removed as for specimen C3. Despite the reduced thickness of the upper portion and the removal of the top surface, crushing was again initiated at the flanges. Consistently with the behavior observed in V1, following an initial stable crushing of the lower section, a major fracture developed at mid-height, just above the tapering (see Figure 4d) and propagated towards the top, eventually separating the specimen into two parts and damaging the upper edge as well. Overall, the introduction of variable thickness induced complex buckling patterns and stress concentrations near the thickness transition, weakening the structure as crushing progressed from the lower edge. As a result, crushing initiated in the thicker lower region, while the thinner upper walls fractured abruptly once the lower section was severely damaged.

The acceleration and force curves from the first three tests are shown in Figure 5a: as a function of displacement and Figure 5b as a function of time. As prescribed by the LMPH 2020 regulation [40], a CFC60 filter was applied, to have a reasonable estimation of the load felt by the pilots, after the propagation of the stress waves in the structures, which acts as a filter. In this case, poor energy absorption is evident in the curves of both the specimens. In particular, as crushing initiated, the load profile rapidly decreased due to the destabilization of the lateral walls. Finally, a pronounced deceleration peak was observed for specimen V1, corresponding to its full compaction. For specimen V2, two initial peaks can be identified, which could be associated with the destabilization of the two larger lateral walls collapsing at different times.

The average crushing acceleration/force, together with the four performance parameters (SEA, MA, CFE, and SE), are summarized in Table 6. For V2, the averaging span was again defined by the first inflection point of the acceleration curve, corresponding to the onset of the derivative decrease by the last local maximum before the final load drop was taken as the endpoint. Differently, in the case of V1, the averaging span is limited to 200 mm of stroke to avoid mixing the results related to crushing and the one related to the compaction phase. The averaging span of the two curves is specified in Figure 5a.

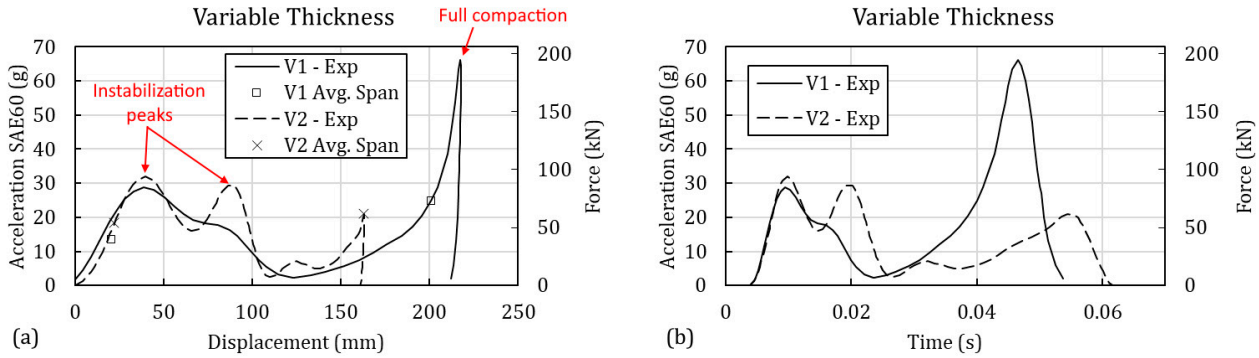

Figure 5. Deceleration curves of variable-thickness specimens, V1 and V2, as a function of (**a**) displacement and (**b**) time.

Table 6. Performance parameters of variable-thickness specimens, V1 and V2.

Specimen	Avg. Crushing Force kN	Max F kN	SEA kJ/kg	CFE kN/kN	SE mm/mm
V1	68.10 ± 49.63	194.50	12.83	0.419	0.98
V2	49.45 ± 24.98	93.93	12.78	0.494	0.74

The average crushing force of specimen V2 was consistent with those of C1, C2, and C3, whereas a considerably higher value was observed for V1, clearly associated with the complete compaction of the specimen and the corresponding high deceleration peak. For both V1 and V2, a low Crushing Force Efficiency (CFE) was obtained, indicating poor stability of the crushing behavior. Conversely, the higher Specific Energy (SE) values can be attributed to the lower force levels.

Concluding, the constant-thickness crash boxes exhibited stable energy absorption but were consistently affected by inverse crushing, triggered at the lower edge due to local stress concentrations at the flange joints. The removal of the top surface proved effective only in reducing the mass, without improving the crushing initiation. Furthermore, the introduction of variable thickness promoted detrimental failure mechanisms, such as large fractures and unstable collapse, thereby reducing the overall effectiveness of energy dissipation. Nevertheless, this experimental characterization of the crash box crushing behavior provides a valuable basis for the calibration of a numerical model.

3. Numerical Modeling

Finite Element (FE) modeling of composite crushing is well known to be a challenging task due to the presence and combination of multiple damage mechanisms, both intra- and interlaminar, associated with the fibers, the matrix, or their interface. Different length scales and levels of idealization can be adopted depending on the desired outcome. Considering the objective of implementing an optimization procedure that requires hundreds of analyses, a modeling approach that is computationally efficient yet capable of effectively capturing the behavior associated with different layups and macroscopic geometric variations is required, such as single-shell element modeling. This technique provides several advantages for the simulation of composite crushing. Its main strength lies in computational efficiency, requiring significantly fewer degrees of freedom than solid elements, which enables large-scale parametric studies and optimization procedures. Additionally, shell elements allow for a convenient representation of thin-walled structures, effectively capturing the global load-displacement response and energy absorption behavior for different layups and geometries. Nevertheless, some limitations should be considered. Shell

models do not provide through-thickness resolution, making the direct simulation of interlaminar failure modes, such as delamination, not possible. They are also sensitive to the calibration of material properties, failure criteria, and contact definitions, which require careful validation to ensure accurate predictions. Moreover, progressive damage mechanisms, including crack initiation, fiber breakage, and matrix cracking, are represented in a simplified manner, potentially reducing fidelity in capturing the detailed sequence of failure. Despite these limitations, shell modeling is a robust and practical approach, and its drawbacks can be mitigated through appropriate parameter calibration, damage modeling techniques, and experimental validation. Indeed, any modeling strategy involving a solid or cohesive element would bring a prohibitive computational cost.

3.1. Model Setup

The FE model was developed in the Simulia/Abaqus 2023 environment using the explicit solver. The specimens were modeled by simplifying the original three-dimensional CAD geometries into two-dimensional surfaces corresponding to their external shapes. Two versions were prepared: the first included the top surface, representing specimens C1, C2, and V1, while the second excluded the top surface, representing specimens C3 and V2. The entire geometry was meshed using S4R elements with an average size of 4 mm. Concerning the mesh size, it should be noted that when material softening is introduced in the FE model, the solution becomes mesh-dependent, with no convergence upon mesh refinement. Therefore, an average element size of 4 mm was chosen as a compromise between computational efficiency and the characteristic length scale of the curved edges and of the observed damage phenomena. Moreover, since all phenomena occurring at length scales smaller than the laminate thickness are already approximated by the adoption of shell elements, further mesh refinement below would not yield additional meaningful information. A picture of the meshes is shown in Figure 6. For the sake of completeness, a mesh sensitivity study was performed comparing the reference 4 mm mesh with versions of 2 mm and 6 mm. The results of the comparison are reported in the Appendix A, and they show how the variation of the performance parameters remains under 10% and that the primary failure mode is captured in the same way. The steel fixture plate and the impactor were modeled as rigid analytical surfaces, with a concentrated mass of 300 kg assigned to the latter.

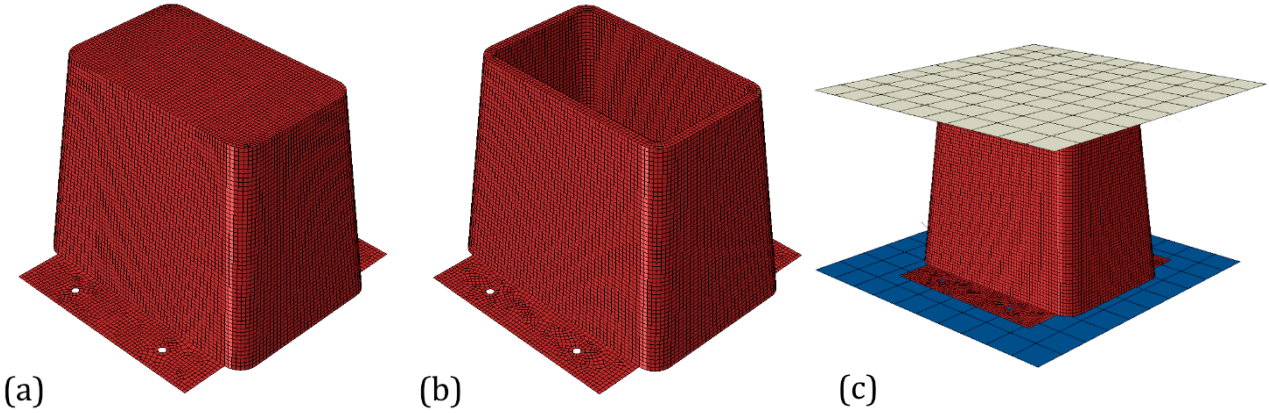

Figure 6. Geometry and mesh of the specimen (**a**) before and (**b**) after the top surface removal, and (**c**) the complete configuration of the model with the support and impacting surfaces.

The specimen was fixed to the rigid steel fixture by applying four constraints in the flange regions corresponding to the screw holes. All degrees of freedom of the fixture were constrained, while for the impactor only the vertical translation was left free, and an initial vertical velocity equal to that measured in the experimental tests was imposed.

A contact law was defined among all model parts, including self-contact, with a "hard" normal behavior (infinite penalty stiffness) and a Coulomb friction tangential component with a friction coefficient of 0.1, as many times used in literature [24,28,41].

A composite shell section was defined with several integration points stacked through the thickness: each ply is represented by three of them. For the two composite materials adopted, A and B, a plane-stress orthotropic stiffness matrix was defined. The elastic properties were provided by the manufacturer, and they are in the typical range of commercially available carbon/epoxy composites [42]. In the present case, the 2D Hashin damage criterion was adopted to model the crushing of the composite. This model is actually the composition of four damage initiation criteria: tensile F_L^T and compressive longitudinal damage, tensile and compressive transversal damage, and each of them can be influenced by the presence of shear stress. When one of them is met, the correspondent scalar damage variable starts increasing, reducing the correspondent element of the stiffness tensor, such that the maximum stress bearable by the material decreases linearly up to zero, when the material is considered failed and the element is deleted. More details on the implementation can be found in the Abaqus manual [43].

As experimentally observed, composites crush with a composition of damage mechanisms, intra- and interlaminar, related to the matrix, fibers, or interface between them. As already mentioned, one of the main limitations of adopting a single-shell technique is the impossibility of modeling interlaminar damage. Nonetheless, the energy-dissipation contribution of this damage mechanism can be considered by artificially increasing the fracture toughness of other damage modes, which can be captured by the single-shell model, typically the in-plane compressive damage.

After a sensitivity study of the strengths and toughness, a set was adopted, which is in line with the data available in the literature [42]. The elastic properties and Hashin damage law parameters used are reported in Table 7. It must be specified that these tuned parameters are not strain-rate sensitive, so they are calibrated assuming an constant averaged strain-rate during the impact.

Table 7. Calibrated values of elastic properties and damage parameters adopted.

		Material A	**Material B**
Elastic Properties	$E_{11} = E_{22}$	58 GPa	57.3 GPa
	G_{12}	4.3 GPa	4.5 GPa
	$G_{13} = G_{23}$	2.58 GPa	2.7 GPa
	v_{12}	0.047	0.041
Hashin Damage Law	Strength		
	$s_{11}^T = s_{22}^T$	710 MPa	897.8 MPa
	$s_{11}^C = s_{22}^C$	510 MPa	429.7 MPa
	s_{12}	86 MPa	90 MPa
	Fracture Toughness		
	$K_{11}^T = K_{22}^T$	125 J/m^2	125 J/m^2
	$K_{11}^C = K_{22}^C$	245 J/m^2	245 J/m^2

T.b.n.: where T and C apexes stand for Traction and Compression.

One of the main issues associated with this modeling technique is the frequent distortion of elements located at the crushing front. When the scalar damage variable approaches values close to one within a given element, its effective stiffness tends toward zero. As a consequence, the element becomes unrealistically compliant and may undergo severe distortion even under realistic load levels. To mitigate this issue, element deletion can be triggered at damage values lower than one, so that elements are removed before becoming

excessively compliant. The drawback of this approach is a reduction in the total fracture energy, which may affect the accuracy of the simulation. Therefore, this technique must be carefully calibrated to prevent non-physical results. In the present work, the damage threshold for element deletion was set to 0.99.

3.2. Correlation

The average computational time necessary to run the analyses using 10 Intel(R) Xeon(R) Gold 6338 CPUs @ 2.00 GHz was ∼15 min. The correlation between the experimental results and the numerical curves obtained using the calibrated model (with material properties reported in Table 7) is shown in Figure 7. As in the experimental setup, a CFC60 filter was applied to the acceleration signals. The comparison was carried out in terms of acceleration/force versus displacement and versus time, for both constant- and variable-thickness specimens. In all cases, the numerical simulations reproduce the experimental response with good accuracy. For constant-thickness specimens, the numerical plateau exhibited a slightly less stable behavior, which may be attributed to the fact that the adopted constitutive law neglects the viscous damping associated with material crushing. Although this effect is not dominant, it can still influence plateau stability.

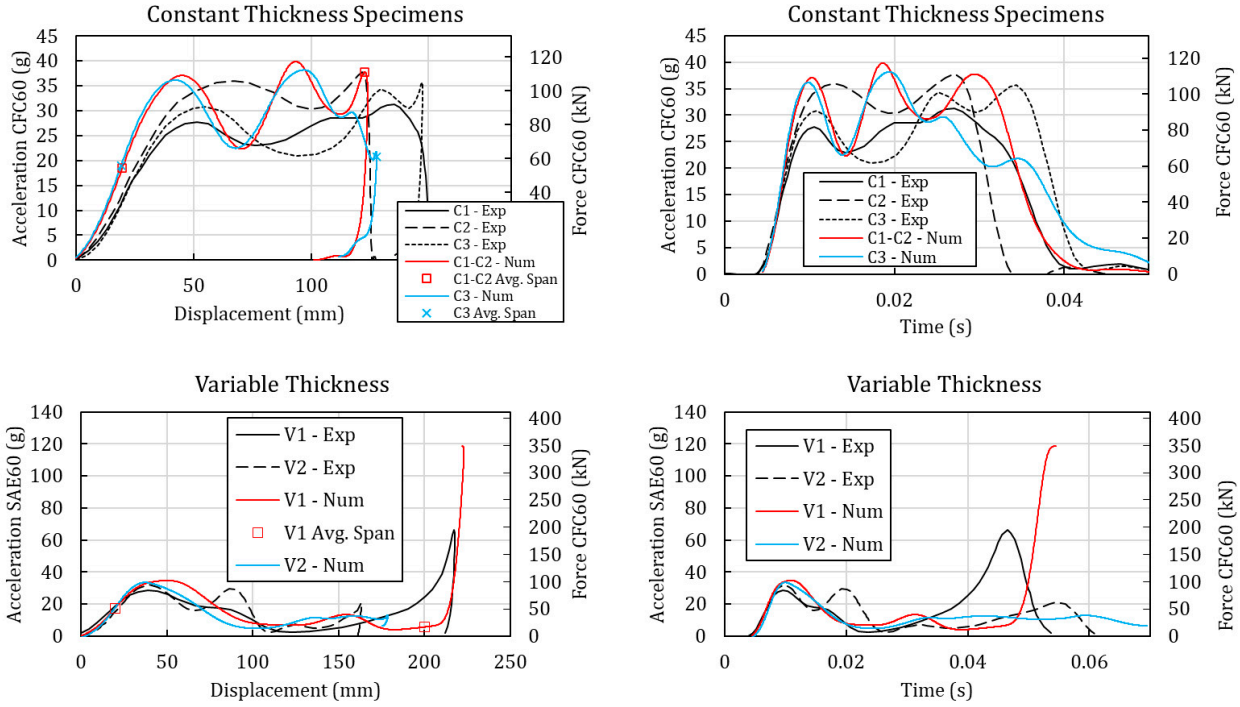

Figure 7. Comparison between the experimental and numerical deceleration curves for constant-thickness and variable-thickness specimens.

For the variable-thickness specimen (V1), the model overestimated the compaction, both in terms of the stroke and reaction force. Nevertheless, this discrepancy is reasonable, as a single-shell modeling approach cannot fully capture this effect without explicitly accounting for the out-of-plane stress components.

From a morphological standpoint, a satisfactory correlation between experimental and numerical results was achieved, as shown in Figure 8. For all tests, the inverse crushing mode observed experimentally was successfully reproduced by the numerical model, along with the corresponding macroscopic failure patterns. For C1/C2 and C3, the model accurately captured the stable inverse crushing behavior triggered by the flanges, and the size and distribution of the fractured pieces were found to be comparable to the experimental observations. In the case of V1 and V2, the numerical model effectively

reproduced the initial inverse crushing phase, followed by the instability of the larger side walls and the final collapse of the curved regions. Moreover, as highlighted in Figure 8, the diagonal cracking observed on the lateral walls was accurately predicted by the simulation. The contours of compressive damage in the outer composite layer, presented in Figure 8, suggest that, in C1/C2 and C3, the flanges are the first elements to fail, followed by an instability in the lower part of the two larger walls, ultimately leading to a bending failure. This may explain the formation of the stripe-shaped debris observed experimentally. In Figure 8, two arc-shaped damage patterns can be seen on the larger walls at locations where instability occurs. For V1 and V2, the damage patterns indicate an instability of one of the four curved vertical edges, a few centimeters above the tapering, where the wall is thinner. The figure shows a concentration of damage in this region.

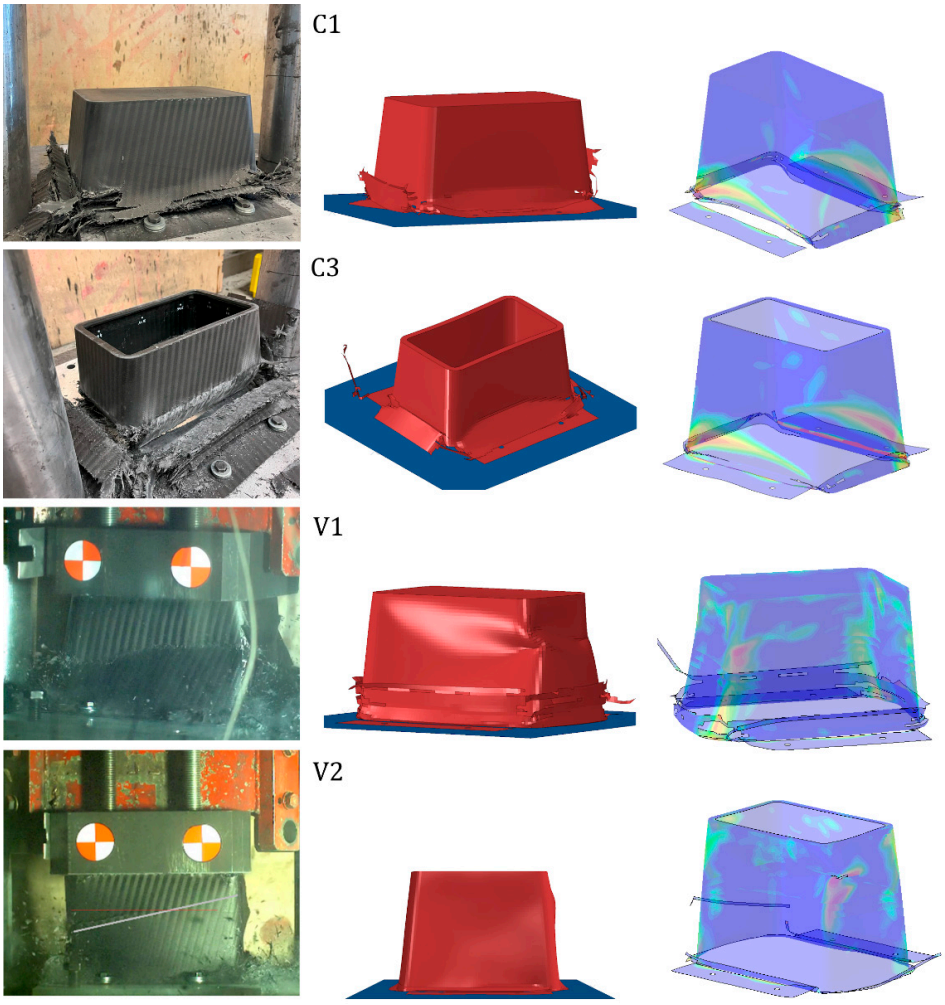

Figure 8. Morphological comparison between the experimentally and numerically observed crushing modes in specimens C1, C3, V1, and V2. On the right, the contours of the damage variable related to compression in 0° direction (blue = 0.00, red = 0.95).

The correlation of performance parameters is presented in Figure 9, expressed in terms of the errors between experimental and predicted values. The averaging spans were determined in the same manner as for the experimental data and are reported in Figure 7. As before, for specimen V1, the averaging span was interrupted at 200 mm of stroke to avoid including the compaction phase. For specimens C1 and C3, all the calculated errors were below 10%, which represents a remarkable agreement, considering the level of approximation introduced by the adopted modeling strategy. The largest deviations were observed for V1 and V2, which overestimated the initial peak force. This discrepancy may

be attributed to the simplified modeling of the tapering geometry, potentially leading to a slight overprediction of material strength. Overall, when averaging across all specimens, errors below 10% were obtained for all performance parameters, except for the maximum and average force, for which the errors remained below 15%.

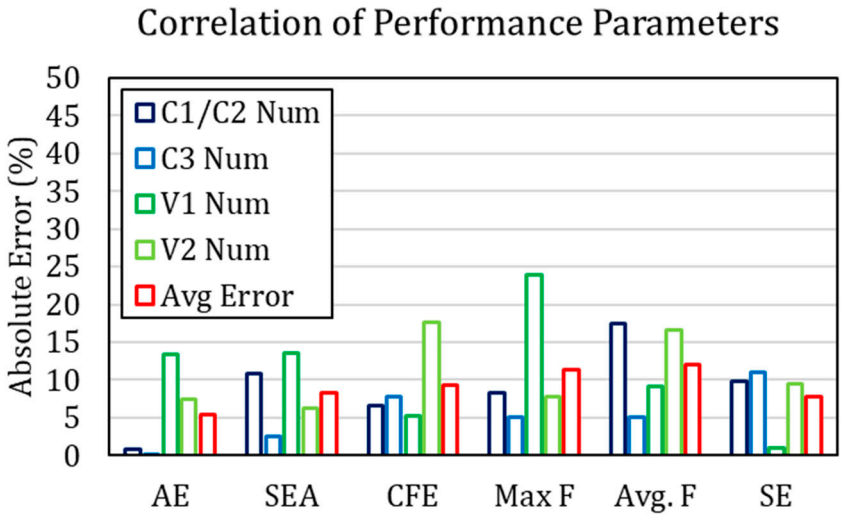

Figure 9. Absolute percentual error between the experimental and numerical values of the performance parameters.

To clarify the influence of the Hashin failure parameters, a sensitivity analysis was conducted and is reported in Appendix A (see Figure A1). In this analysis, the acceleration curves obtained by increasing and decreasing, by 10%, the tensile and compressive strengths, s_{11}^T and s_{11}^C (equal to s_{22}^T and s_{22}^C) and the tensile and compressive fracture toughnesses K_{11}^T and K_{11}^C (equal to K_{22}^T and K_{22}^C) were compared with the curve obtained using the reference parameters listed in Table 7.

4. Optimization

4.1. Geometry

Once a reliable and lightweight numerical model was developed and validated against the experimental results, it was employed to optimize the crash box geometry with the aim of preventing the inverse crushing behavior consistently observed in previous tests, thereby improving the overall crushing performance. To this end, three geometric modifications were proposed. As previously discussed, both experimental and numerical results indicated that the inverse crushing mode was initiated by stress concentrations in the region where the flanges connect to the lateral walls. In fact, the contact between the lower edge and the metallic support plate was not perfectly uniform. Therefore, in the first modification, the flanges were made continuously along the entire perimeter of the crash box, ensuring a full connection with the side walls in order to uniformly distribute the impact load over a larger area. Secondly, the upper surface was completely removed, eliminating the 10 mm peripheral frame used in the C3 and V2 specimens, which could otherwise hinder the initiation of crushing on the top face. In fact, the remaining flange could act as a reinforcement against the delamination, thus the crushing, of the first millimeter of lateral walls, where the crushing is desired. Finally, a cruciform reinforcement was introduced inside the crash box. Its purpose was to increase the flexural stiffness of the lateral walls, reducing their free deflection length, and thereby raise their instability load, promoting a stable progressive crushing mode rather than a global buckling collapse. The geometry of this new specimen, named O1, is presented in Figure 10a.

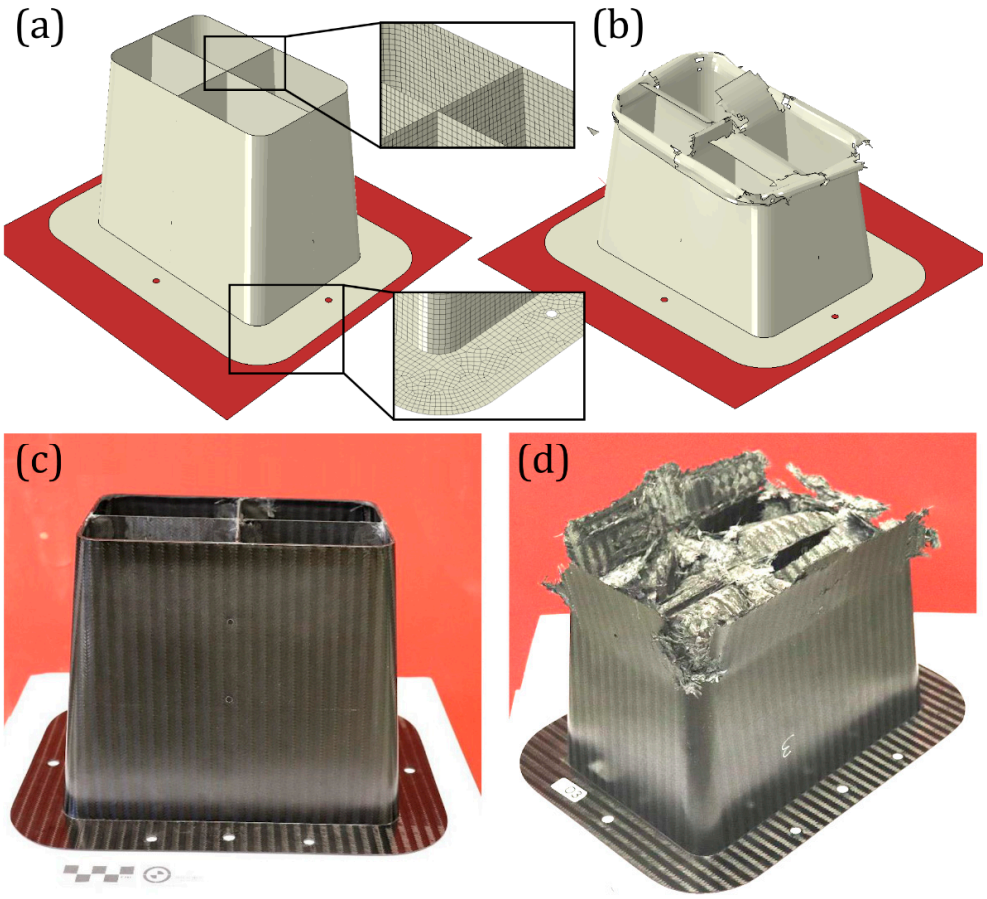

Figure 10. Improved geometry with continuous flanges and cruciform, before and after the impact, in the numerical case (**a**,**b**) and in the experimental case (**c**,**d**).

Based on the experimental results, a constant wall thickness was selected. Since the presence of the cruciform reinforcement was expected to significantly increase the crushing force, the number of plies in the lateral walls was reduced from eight to six. Three piles were used for both the cruciform and the flanges. The complete stacking sequence of the optimized specimen geometry is reported in Table 8.

Table 8. Optimized geometry specimen O1 lay-up, from outer to inner layers.

	Region	Fabric	Orientation
Ply-1	Side walls + Flanges	A	45°
Ply-2	Side walls + Flanges	B	45°
Ply-3	Side walls + Flanges	B	0°
Ply-4	Side walls	B	0°
Ply-5	Side walls	B	45°
Ply-6	Side walls	A	45°
Ply-7	Cruciform	A	45°
Ply-8	Cruciform	A	0°
Ply-9	Cruciform	A	45°

The new specimen was produced and tested following the same procedure described previously. The quantitative results are reported in Table 9, while images of the specimen before and after testing are shown in Figure 10c,d. As anticipated, the introduction of the continuous flange enabled proper crushing initiation from the upper surface. The impacted specimen exhibited stable crushing with delamination occurring through both the lateral walls and the cruciform, splitting the panels into two layers that collapsed by bending.

The presence of the cruciform increased the mass, the peak value and average crushing forces, resulting in an improved SEA. Consequently, a shorter stroke was required to stop the impactor.

Table 9. Performance parameters of specimen O1.

	Mass kg	Avg. Crushing Force kN	Max F kN	SEA kJ/kg	CFE kN/kN	SE mm/mm
O1	1044	146.50 ± 51.36	194.64	42.56	0.75	0.40
Variation with respect to C3	15.7%	78.51%	85.48%	113.65%	−4.09%	−40.30%

The impact test on this new specimen was first simulated to verify whether the numerical prediction confirmed the expected outcome. The numerical model was set up following the same procedure adopted for the previous configurations. A picture of the model, before and after the impact, is presented in Figure 10a,b. In light of the intrinsic limitation of the numerical technique, namely its inability to capture delaminations, the morphological outcome of the model appears satisfactory, faithfully replicating the experimental observations.

Figure 11 shows a comparison between the experimental and numerical acceleration curves as functions of displacement and time. Compared to the previous specimens (see Figure 3), the loads involved are considerably higher, and the impact duration is approximately half. The numerical curves accurately reproduce the slope—reflecting the stiffness—and the area under the curves but tend to underestimate the peak force. This discrepancy can be attributed to the cruciform, whose crushing behavior is modeled as almost pure bending, thereby neglecting the panel-splitting mechanism and the force contribution arising from the self-interaction of crushing fragments at the delamination front. For this reason, the correlation error of the maximum forces and CFE have an error around 15%. All the other performance parameters remain below 10%, further validating the numerical approach.

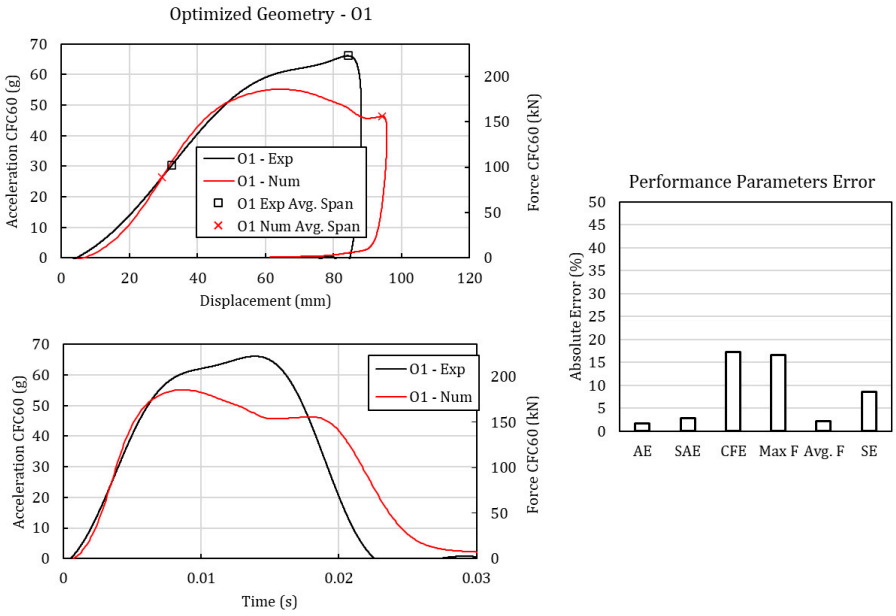

Figure 11. Experimental and numerical curves for the impact test of O1 specimen, with correlation error.

4.2. Layup

The proposed geometric modifications resulted in the desired crushing mode and a significant increase in the specific energy absorption (SEA). Furthermore, the new experimental tests provided additional validation of the numerical model. However, the higher SEA was accompanied by an increase in the mean crushing force and a reduction in stroke efficiency. Therefore, the next step in improving the crash box performance was the optimization of the laminate layup, aiming to exploit the maximum possible stroke while minimizing the average crushing load.

The selected modeling technique presented some limitations due to the high idealization and approximation level, as it was previously discussed. Nonetheless it allowed a lightweight model, which can be used for approaches that require hundreds of analyses. For this reason, a genetic algorithm was implemented using the built-in Matlab® 2024 function, which varied the orientation of each ply in the crash box to identify the optimal configuration. For the optimization to be effective, it was essential to define an appropriate error function to be minimized. To achieve a more efficient energy absorber, the objective function was defined as follows:

$$e = \frac{\overline{\sigma}}{SE}$$

where SE is the maximum stroke efficiency, σ is the standard deviation of the acceleration curve, and $\overline{\sigma}$ is the σ measured for the current configuration, normalized based on the σ of the initial reference configuration with all the orientation angles being 0°. In this way, both SE and $\overline{\sigma}$ range around [0,1] (to be noted: SE can be only inside [0,1], $\overline{\sigma}$ can exceed 1 but should reasonably maintain values close to it), thus having a similar weight in the optimization. By minimizing e, the best compromise between maximizing the stroke and ensuring the stability of the crushing load is achieved, thus approaching the behavior of an ideal energy absorber, for which $\sigma = 0$ with the lowest possible average force. If the absorber is unable to stop an impactor with kinetic energy K, the residual energy leads to an impact with the rigid floor, producing a large force peak that significantly increases $\overline{\sigma}$ and penalizes the solution. If the absorber successfully stops the impactor, energy conservation requires that the integral of the crushing force over the displacement equals K. Under this condition, an optimal solution is characterized by the maximum effective stroke, which corresponds to a lower average crushing force and reduced force fluctuations. The genetic algorithm was initialized with a population of fifty individuals and allowed to evolve for a maximum of eleven generations. It is important to note that the stopping criterion was based on the maximum number of generations rather than on convergence. This choice was made considering the high computational cost of explicit finite element analyses, even for relatively lightweight models. The average time for a single analysis was around 1.5 h, resulting in more than 800 h for the total procedure. For this reason, waiting for full convergence of e would have resulted in unreasonably long computation times. Therefore, it cannot be claimed that the obtained configuration represents the absolute optimum. Nevertheless, after eleven generations, the solution achieved a substantial improvement in performance.

For manufacturing considerations, the possible orientation angles of each ply were limited to 0°, 15°, 30°, 45°, 60°, and 75°. Under the assumption of a transversely isotropic stiffness matrix, the material response is invariant under 90° rotations. Therefore, the selected angles effectively cover the entire 360° range. In Figure 12, the value of e of each individual in each generation is reported. Then, the evolution of the best solution for each generation was indicated by the red line. After seven generations, a minimum value was reached, which remained stable for the further four. In the end, a reduction of e of 10.53% was obtained with respect to the minimum of the first generation, 4.04%, compared to the

full 0° configuration, and 30.54%, compared to one obtained from the lamination sequence of O1.

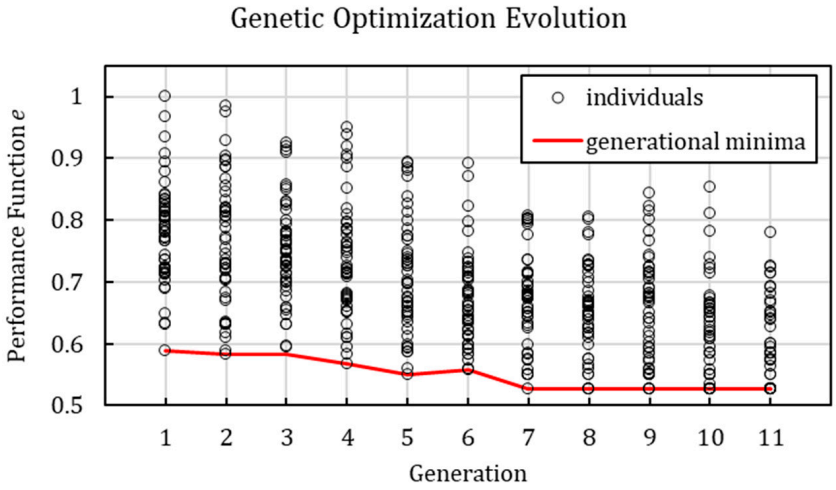

Figure 12. Objective function *e* with the increasing number of generations.

The optimal lamination sequence is reported in Table 10. It is difficult to establish a clear correlation between orientation angles and absorber performance, due to the interaction of complex elastic and inelastic effects. However, considering that 0° corresponds to the longitudinal direction, the optimized specimen exhibits a stiffer layup with smaller angles compared to O1, which may be associated with a more brittle response. It can be hypothesized that the outer 0°-oriented plies are, to some extent, stabilized by the presence of inner off-axis plies, acting synergistically.

Table 10. Optimal layup identified by the genetic algorithm.

	Region	Fabric	Orientation
Ply-1	Side walls + Flanges	A	0°
Ply-2	Side walls + Flanges	B	0°
Ply-3	Side walls + Flanges	B	0°
Ply-4	Side walls	B	15°
Ply-5	Side walls	B	30°
Ply-6	Side walls	A	45°
Ply-7	Cruciform	A	15°
Ply-8	Cruciform	A	15°
Ply-9	Cruciform	A	0°

The comparison among the deceleration curves of O1 specimens, of a reference configuration Full_0° with only 0° plies, and the one with the optimal layup is presented in Figure 13, clearly showing the improvement. The optimal curve shows a stable crushing profile, lower than the ones of Full_0° and O1, with a longer stroke. Nonetheless, a slightly descending profile slope signs that a further optimization margin is possible. In Figure 13, the percentage variation of the performance parameters is reported, showing how both the maximum and the average forces decreased, with an increase of the crush force efficiency and stroke efficiency. It is relevant to note that, in this case, the decreased SEA is linked to improved performance.

Figure 14 compares the damage morphologies in the first composite layer during the initial stages of crushing for the Full_0°, O1, and Opt specimens. This comparison highlights a clear concentration of damage at the flanges, associated with excessive bending stresses. At the crush front, the dominant damage mechanism is tensile failure in

the 0° direction. Although, under the adopted assumptions, the absorbed in-plane energy also includes contributions from interlaminar damage—which the model cannot capture explicitly—the observed trends remain meaningful. The higher performance of the Opt specimen and partially of the Full_0° specimen, which is stiffer than O1, appears to be related to a more distributed damage pattern in the lateral and cruciform walls (clearly visible in the 0° compression and shear damage contours), together with a reduced damage concentration at the flanges. In contrast, the flange damage concentration is most pronounced in the O1 specimens.

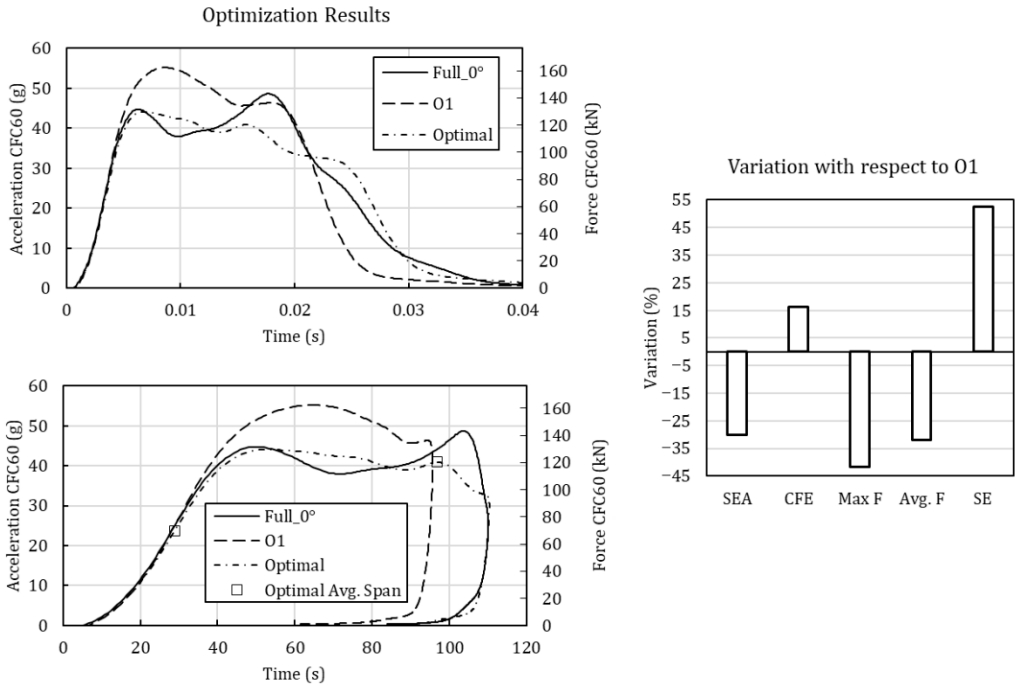

Figure 13. Deceleration curves of the specimen with the optimal layup, compared with O1 and a reference configuration Full_0°, and the performance parameter variation with respect to O1.

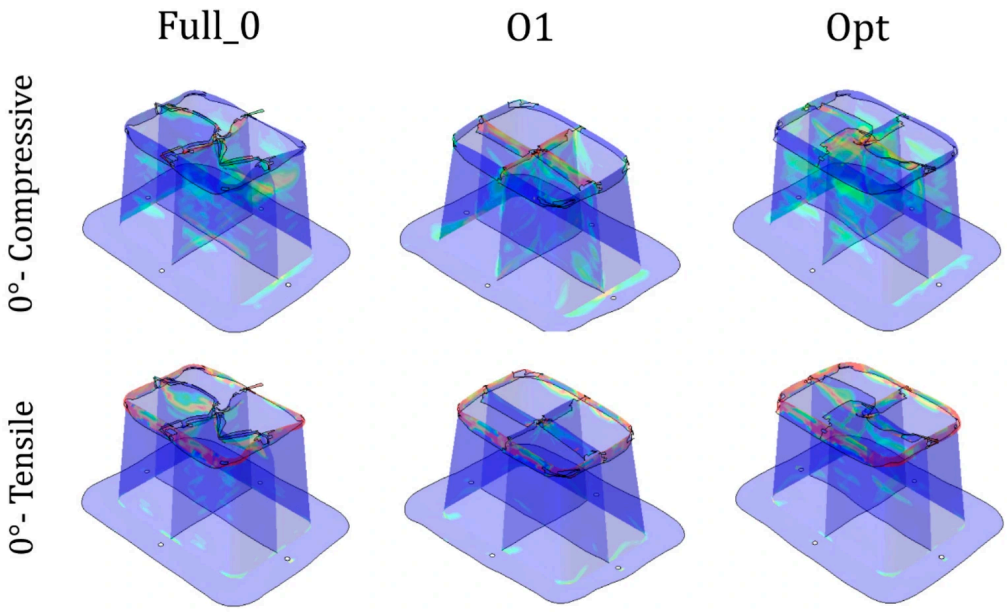

Figure 14. *Cont.*

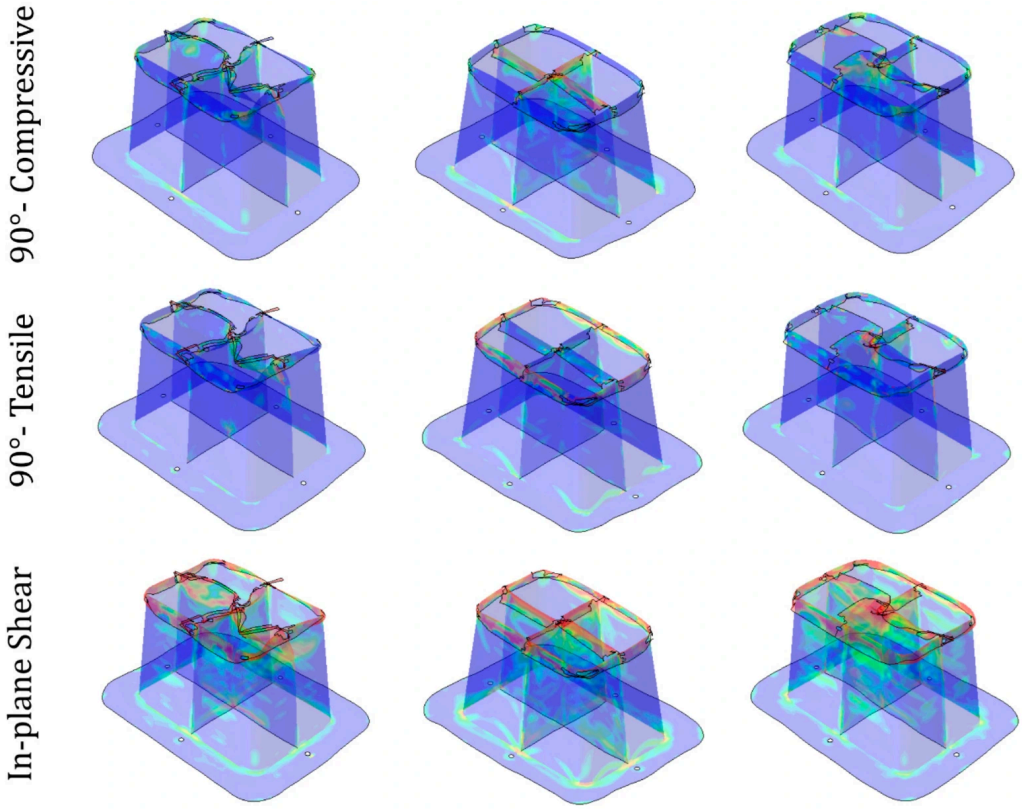

Figure 14. Contour of damage variables related to compressive, tensile, and shear in 0° and 90° direction for Full_0°, O1, and Opt specimens (blue = 0.00, red = 1.00).

5. Conclusions

This work presented a hybrid experimental–numerical approach for the preliminary design optimization of a CFRP crash box intended for high-performance automotive applications. The experimental campaign highlighted the influence of geometric features and layup configurations on the crushing behavior and energy-absorption capability. Constant-thickness specimens exhibited stable performance but were consistently affected by inverse crushing, triggered by local stress concentrations at the flange joints. Conversely, variable-thickness configurations promoted detrimental failure mechanisms, such as large fractures and unstable collapse, reducing the overall efficiency.

A lightweight finite element model based on shell elements was developed and calibrated against experimental results, achieving errors below 10% for most performance parameters and below 15% for peak forces. Despite its intrinsic limitations, such as the inability to capture delamination, the model proved effective in reproducing global crushing behavior and served as a reliable tool for optimization.

Geometric modifications, including continuous flanges, removal of the top surface, and the introduction of a cruciform reinforcement, successfully eliminated inverse crushing and significantly improved specific energy absorption (SEA), even if at the cost of higher mean crushing forces and reduced stroke efficiency. To address this trade-off, a genetic algorithm was implemented to optimize the laminate layup. The resulting configuration achieved a more stable crushing profile, reduced peak and average forces, and improved stroke efficiency, confirming the potential of numerical optimization in enhancing crash box performance.

Overall, the proposed methodology demonstrates that combining experimental validation with computationally efficient modeling enables rapid design iterations and the effective optimization of composite crash absorbers.

Author Contributions: Conceptualization, A.M.C. and G.J.; Methodology, A.M.C. and A.A.; Software, A.M.C. and A.A.; Validation, A.M.C. and A.A.; Formal analysis, A.M.C. and A.A.; Investigation, A.M.C. and A.A.; Data curation, A.M.C. and A.A.; Writing—original draft, A.M.C.; Writing—review & editing, A.A. and G.J.; Visualization, A.A.; Supervision, G.J.; Project administration, G.J.; Funding acquisition, G.J. All authors have read and agreed to the published version of the manuscript.

Funding: This research received no external funding.

Data Availability Statement: The raw data supporting the conclusions of this article will be made available by the authors on request.

Acknowledgments: The authors gratefully acknowledge Pagani Automobili S.p.A. for providing all the test specimens used in the experimental activities.

Conflicts of Interest: The authors declare no conflict of interest. Pagani Automobili S.p.A. had no role in the design of the study; in the collection, analyses, or interpretation of data; in the writing of the manuscript; or in the decision to publish the results.

Appendix A

In the table and figure below, the parameters and curves of the sensitivity study on Hashin parameters are reported. In each set of analyses, a single parameter (in red) was increased or decreased by 10% with respect to the reference configuration. This study is intended to give to the reader awareness of the influence of each parameter on the curves.

Table A1. Hashin damage law parameters for all the analyses performed in the sensitivity study. In red the variation with respect to the reference configuration.

	Compressive Strength (MPa)		**Tensile Strength (MPa)**		**Compressive Toughness (J/m^2)**		**Tensile Toughness (J/m^2)**	
Material	A	B	A	B	A	B	A	B
Reference	710	897.8	510	429.7	245	245	125	125
Comp. Str. +10%	781	987.58	510	429.7	245	245	125	125
Comp. Str. −10%	639	808.02	510	429.7	245	245	125	125
Tens. Str. +10%	710	897.8	561	472.67	245	245	125	125
Tens. Str. −10%	710	897.8	459	386.73	245	245	125	125
Comp. Tough. +10%	710	897.8	510	429.7	269.5	269.5	125	125
Comp. Tough. −10%	710	897.8	510	429.7	220.5	220.5	125	125
Tens. Tough. +10%	710	897.8	510	429.7	245	245	137.5	137.5
Tens. Tough. −10%	710	897.8	510	429.7	245	245	112.5	112.5

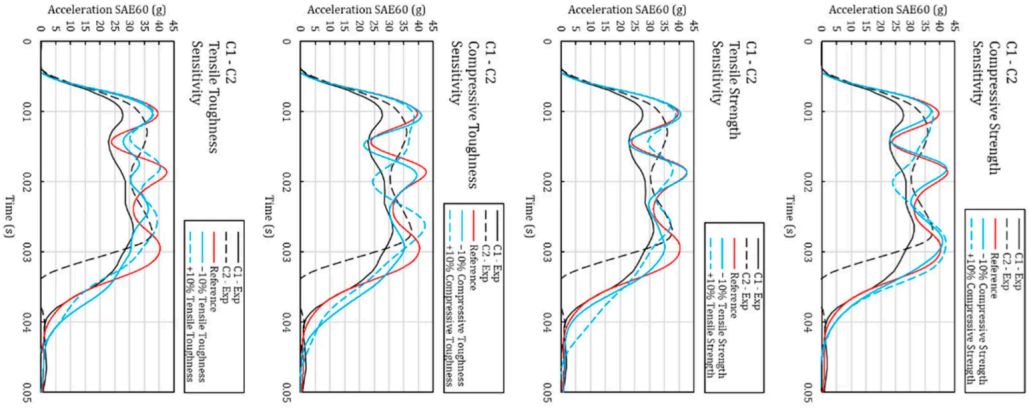

Figure A1. *Cont.*

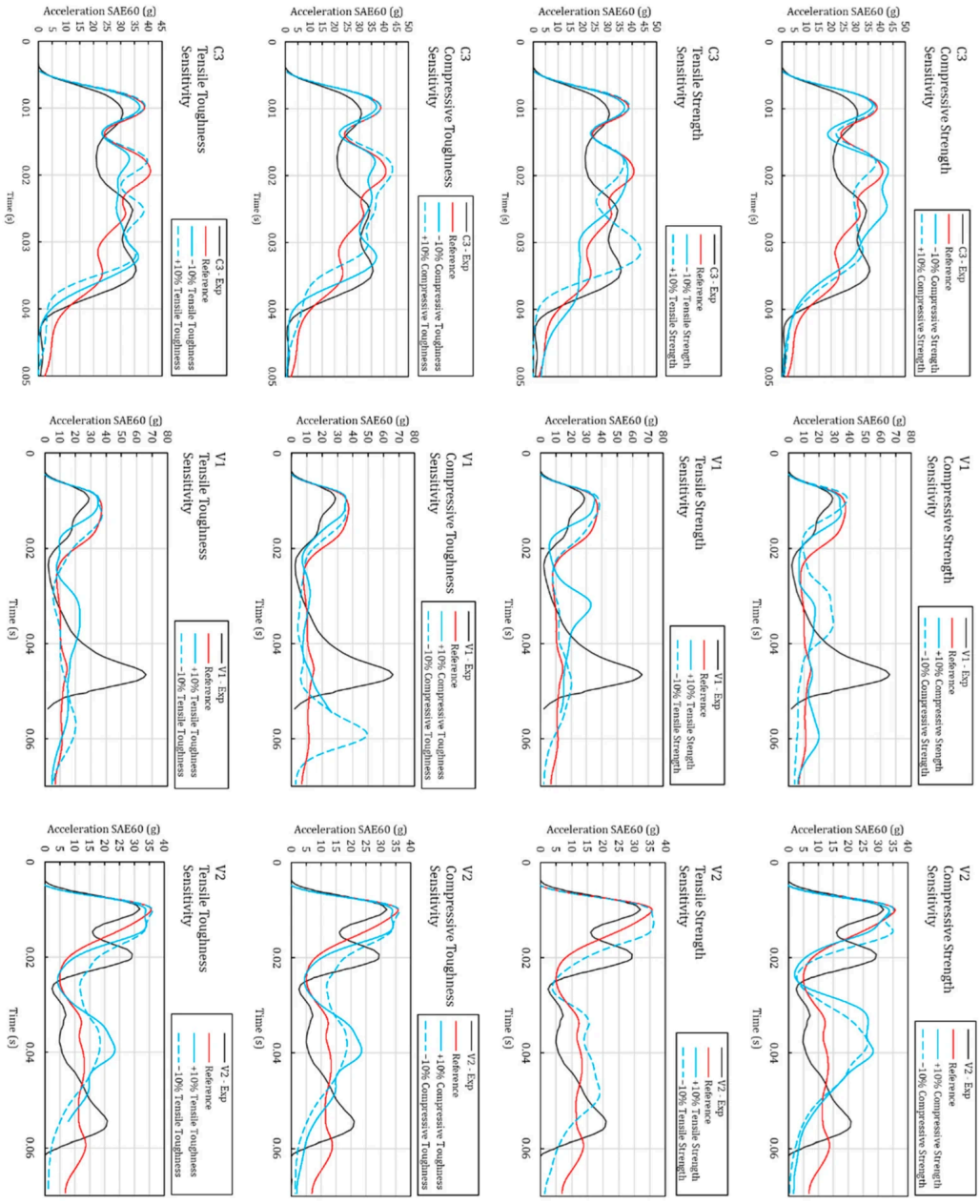

Figure A1. Sensitivity on the deceleration curves of the Hashin strength and toughness parameters. The parameters adopted for each analysis are reported in Table A1.

Even if, as explained in the Section 3, in a Finite Element problem like the present one, which includes material softening behavior, the convergence of the result upon mesh refinement is not guaranteed, a mesh sensitivity study is here reported to give the reader the chance to evaluate the dependance of the result on the average element size. The numerical model of the C1 specimen test was recreated with an average element size of 2 mm and 6 mm, to be compared with the reference one, which has a mesh size of 4 mm. Key performance parameters were compared. The results are reported in Table A2 showing how variation of the parameters never exceeds 10%. In Figure A2, decelerations and the primary failure mode were compared showing comparable results.

Table A2. Sensitivity of the mesh dimension on key performance parameters.

		Reference—4 mm	2 mm	% Var.	6 mm	% Var.
Max F	kN	120.28	108.83	9.52	116.09	3.48
Avg. Crushing Force	kN	96.90	92.00	5.06	87.65	9.55
AE	kJ	10.17	10.31	1.40	10.03	1.34
SE	-	0.56	0.56	0.17	0.61	8.47

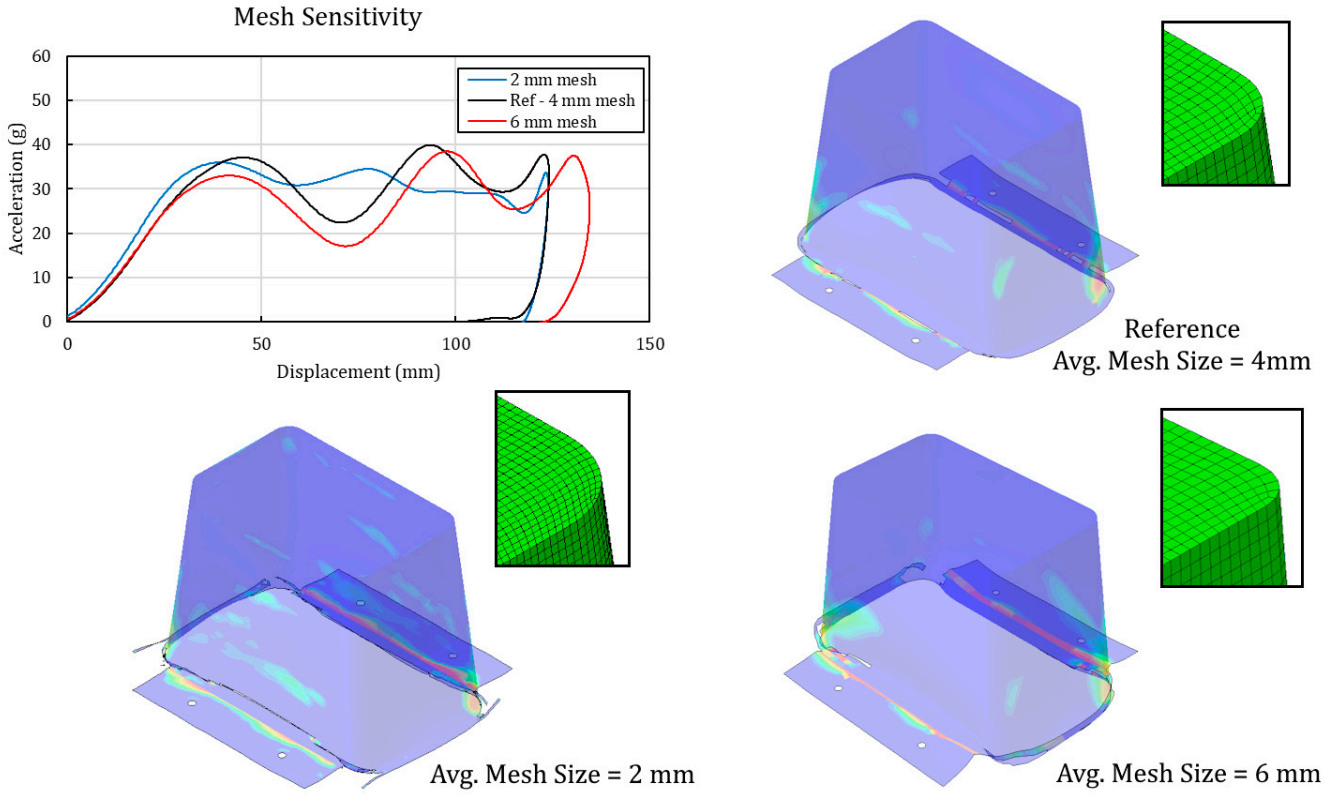

Figure A2. Sensitivity of the mesh size on the deceleration curve and primary failure mode of specimen C1.

References

1. Yusof, N.S.B.; Sapuan, S.M.; Sultan, M.T.H.; Jawaid, M.; Maleque, M.A. Design and materials development of automotive crash box: A review. *Ciência Tecnol. Mater.* **2017**, *29*, 129–144. [CrossRef]
2. Saenz-Dominguez, I.; Tena, I.; Esnaola, A.; Sarrionandia, M.; Torre, J.; Aurrekoetxea, J. Design and characterisation of cellular composite structures for automotive crash-boxes manufactured by out of die ultraviolet cured pultrusion. *Compos. Part B Eng.* **2019**, *160*, 217–224. [CrossRef]
3. Bandinelli, F.; Ciampaglia, A.; Ciardiello, R.; Peroni, L.; Peroni, M.; Scapin, M. High strain rate testing of carbon-epoxy laminate crash boxes filled with polymeric cellular 3D-printed cores. *Int. J. Impact Eng.* **2025**, *205*, 105401. [CrossRef]
4. Saber, A.; Amer, A.M.; Shehata, A.I.; El-Gamal, H.A.; Abd_Elsalam, A. Recent Developments in Additively Manufactured Crash Boxes: Geometric Design Innovations, Material Behavior, and Manufacturing Techniques. *Appl. Sci.* **2025**, *15*, 7080. [CrossRef]
5. Hussain, N.N.; Regalla, S.P.; Rao, Y.V.D.; Dirgantara, T.; Gunawan, L.; Jusuf, A. Drop-weight impact testing for the study of energy absorption in automobile crash boxes made of composite material. *Proc. Inst. Mech. Eng. Part L J. Mater. Des. Appl.* **2021**, *235*, 114–130. [CrossRef]
6. Nasir Hussain, N.; Regalla, S.P.; Daseswara Rao, Y.V. Economical method for manufacturing of advanced light weight material crash box for automobiles. *Mater. Today Proc.* **2020**, *27*, 1186–1191. [CrossRef]
7. Zarei, H.; Kröger, M.; Albertsen, H. An experimental and numerical crashworthiness investigation of thermoplastic composite crash boxes. *Compos. Struct.* **2008**, *85*, 245–257. [CrossRef]

8. Erkek, B.; Kosedag, E.; Adin, H. The impact of graphene filler on the energy absorption of hybrid composite crash boxes. *Int. J. Mech. Mater. Des.* **2025**, *21*, 339–355. [CrossRef]
9. Erkek, B.; Kosedag, E.; Adin, H. Hybridization effect on energy absorption capacity of composite crash boxes. *Polym. Compos.* **2024**, *45*, 12349–12361. [CrossRef]
10. Ghamarian, A.; Zarei, H.R.; Abadi, M.T. Experimental and numerical crashworthiness investigation of empty and foam-filled end-capped conical tubes. *Thin-Walled Struct.* **2011**, *49*, 1312–1319. [CrossRef]
11. Hou, W.; He, P.; Yang, Y.; Sang, L. Crashworthiness optimization of crash box with 3D-printed lattice structures. *Int. J. Mech. Sci.* **2023**, *247*, 108198. [CrossRef]
12. Günaydın, K.; Gülcan, O.; Türkmen, H.S. Experimental and numerical crushing performance of crash boxes filled with re-entrant and anti-tetrachiral auxetic structures. *Int. J. Crashworthiness* **2023**, *28*, 649–663. [CrossRef]
13. Susanth K, S.; Murugan, R.; Raja S, C.; Doutre, P.-T.; Vignat, F. Design and Analysis of an Automotive Crash Box Using Strut-Based Lattice Structures. *J. Comput. Nonlinear Dyn.* **2024**, *19*, 121006. [CrossRef]
14. Özen, İ.; Gedikli, H.; Aslan, M. Experimental and numerical investigation on energy absorbing characteristics of empty and cellular filled composite crash boxes. *Eng. Struct.* **2023**, *289*, 116315. [CrossRef]
15. Jusuf, A.; Jarwadi, M.H.; Hastungkorojati, D.G.; Gunawan, L.; Akbar, M.; Zakaria, K.; Izzaturrahman, M.F.; Palar, P.S. Design Exploration and Optimization of a Multi-Corner Crash Box under Axial Loading via Gaussian Process Regression. *IJTech* **2024**, *15*, 1749. [CrossRef]
16. Ciampaglia, A.; Fiumarella, D.; Boursier Niutta, C.; Ciardiello, R.; Belingardi, G. Impact response of an origami-shaped composite crash box: Experimental analysis and numerical optimization. *Compos. Struct.* **2021**, *256*, 113093. [CrossRef]
17. Ciampaglia, A.; Patruno, L.; Ciardiello, R. Design of a Lightweight Origami Composite Crash Box: Experimental and Numerical Study on the Absorbed Energy in Frontal Impacts. *J. Compos. Sci.* **2024**, *8*, 224. [CrossRef]
18. Hwang, Y.-H.; Han, J.-H. Energy absorption optimisation of an origami-shaped crash box under axial loading. *Int. J. Crashworthiness* **2024**, *29*, 132–141. [CrossRef]
19. Omede', B.; Grande, A.M. Parametric optimization of bio-inspired engineered sandwich core. *Mater. Today Commun.* **2024**, *39*, 108632. [CrossRef]
20. Li, S.; Guo, X.; Liao, J.; Li, Q.; Sun, G. Crushing analysis and design optimization for foam-filled aluminum/CFRP hybrid tube against transverse impact. *Compos. Part B Eng.* **2020**, *196*, 108029. [CrossRef]
21. Falzon, B.G. Computational modelling of the crushing of carbon fibre-reinforced polymer composites. *Phil. Trans. R. Soc. A* **2022**, *380*, 20210336. [CrossRef]
22. Rabiee, A.; Ghasemnejad, H. Finite Element Modelling Approach for Progressive Crushing of Composite Tubular Absorbers in LS-DYNA: Review and Findings. *J. Compos. Sci.* **2021**, *6*, 11. [CrossRef]
23. Chiu, L.N.S.; Falzon, B.G.; Boman, R.; Chen, B.; Yan, W. Finite element modelling of composite structures under crushing load. *Compos. Struct.* **2015**, *131*, 215–228. [CrossRef]
24. Chiu, L.N.S.; Falzon, B.G.; Chen, B.; Yan, W. Validation of a 3D damage model for predicting the response of composite structures under crushing loads. *Compos. Struct.* **2016**, *147*, 65–73. [CrossRef]
25. Tan, W.; Falzon, B.G. Modelling the crush behaviour of thermoplastic composites. *Compos. Sci. Technol.* **2016**, *134*, 57–71. [CrossRef]
26. Tan, W.; Falzon, B.G.; Price, M. Predicting the crushing behaviour of composite material using high-fidelity finite element modelling. *Int. J. Crashworthiness* **2015**, *20*, 60–77. [CrossRef]
27. Sokolinsky, V.S.; Indermuehle, K.C.; Hurtado, J.A. Numerical simulation of the crushing process of a corrugated composite plate. *Compos. Part A Appl. Sci. Manuf.* **2011**, *42*, 1119–1126. [CrossRef]
28. Jiang, H.; Ren, Y.; Gao, B. Research on the progressive damage model and trigger geometry of composite waved beam to improve crashworthiness. *Thin-Walled Struct.* **2017**, *119*, 531–543. [CrossRef]
29. Bussadori, B.P.; Schuffenhauer, K.; Scattina, A. Modelling of CFRP crushing structures in explicit crash analysis. *Compos. Part B Eng.* **2014**, *60*, 725–735. [CrossRef]
30. Schrank, M.; Ping, G.; Yingying, P. Simulation of crushing behavior for automotive composites structures. Presented at the China Conference of Automotive Safety Technology, Baoding, China, August 2014. [CrossRef]
31. Patel, D.K.; Pineda, E.J.; Naghipour, P.; Arnold, S.M. Modeling and characterization of crushable composite structures. Presented at the AIAA SCITECH 2023 Forum, Oxon Hill, MD, USA, 23–27 January 2023.
32. Ciampaglia, A.; Fiumarella, D.; Boursier Niutta, C.; Ciardiello, R.; Belingardi, G. Physics based data driven method for the crashworthiness design of origami composite tubes. *Int. J. Mech. Mater. Des.* **2024**, *20*, 445–462. [CrossRef]
33. Qin, X.; Ma, Q.; Gan, X.; Cai, M.; Cai, W. Failure analysis and multi-objective optimization of crashworthiness of variable thickness Al-CFRP hybrid tubes under multiple loading conditions. *Thin-Walled Struct.* **2023**, *184*, 110452. [CrossRef]
34. Boria, S.; Obradovic, J.; Belingardi, G. On design optimization of a composite impact attenuator under dynamic axial crushing. *FME Trans.* **2017**, *45*, 435–440. [CrossRef]

35. Ma, Q.; Zha, Y.; Dong, B.; Gan, X. Structure design and multiobjective optimization of CFRP /aluminum hybrid crash box. *Polym. Compos.* **2020**, *41*, 4202–4220. [CrossRef]
36. Zarei, H.R.; Kröger, M. Crashworthiness optimization of empty and filled aluminum crash boxes. *Int. J. Crashworthiness* **2007**, *12*, 255–264. [CrossRef]
37. Zarei, H.; Kröger, M. Optimum honeycomb filled crash absorber design. *Mater. Des.* **2008**, *29*, 193–204. [CrossRef]
38. Zarei, H.R.; Kröger, M. Optimization of the foam-filled aluminum tubes for crush box application. *Thin-Walled Struct.* **2008**, *46*, 214–221. [CrossRef]
39. Mohammadiha, O.; Beheshti, H.; Aboutalebi, F.H. Multi-objective optimisation of functionally graded honeycomb filled crash boxes under oblique impact loading. *Int. J. Crashworthiness* **2015**, *20*, 44–59. [CrossRef]
40. Fédération Internationale de l'Automobile. *Le Mans Prototype Hypercar Technical Regulations*; Fédération Internationale de l'Automobile: Paris, France, 2020.
41. Liu, H.; Zhou, J.; Zhang, D.; Li, S.; Giannopoulos, I. Effects of contact friction and ply blocking on the crush behaviour of thin-walled composite structures: A numerical study. *Thin-Walled Struct.* **2023**, *182*, 110214. [CrossRef]
42. Indermuehle, K.C.; Sokolinsky, V.S.; Barnes, G. Simulating composites crush: From the coupon level to full vehicle crashworthiness. Presented at the 52nd AIAA/ASME/ASCE/AHS/ASC Structures, Structural Dynamics and Materials Conference 19th AIAA/ASME/AHS Adaptive Structures Conference 2011, Denver, CO, USA, 4–7 April 2011.
43. SIMULIA/Abaqus® 6.6 Manual. Available online: https://classes.engineering.wustl.edu/2009/spring/mase5513/abaqus/docs/v6.6/books/hhp/default.htm?startat=pt01ch01s01.html (accessed on 1 March 2024).